

Single-dopant band bending fluctuations in MoSe₂ measured with electrostatic force microscopy

Megan Cowie,¹ Rikke Plougmann,² Zeno Schumacher,³ and Peter Grütter¹

¹*Department of Physics, McGill University, Montréal, Québec, Canada*

²*Department of Physics, Technical University of Denmark, Lyngby, Denmark*

³*Department of Physics, Institute of Quantum Electronics, ETH Zurich, 8093 Zürich, Switzerland*

(Dated: October 18, 2021)

In this work, we experimentally demonstrate two-state fluctuations in a metal-insulator-semiconductor (MIS) device formed out of a metallic atomic force microscopy tip, vacuum gap, and multilayer MoSe₂ sample. We show that noise in this device is intrinsically bias-dependent due to the bias-dependent surface potential, and does not require that the frequency or magnitude of individual dopant fluctuations are themselves bias-dependent. Finally, we measure spatial nonhomogeneities in band bending (charge reorganization) timescales.

Individual charge state fluctuations have been observed in a variety of electrically isolated systems such as adatoms[1], quantum dots[2, 3], and molecules[4] on insulators. Understanding these systems is critical for the study of single-electron physics, and two-state systems are of particular relevance for emerging quantum information technology. In semiconducting devices, individual charge states such as dangling bonds[5], individual dopants[6], and defects[7] are not electrically isolated from their environment, and it is necessary to understand their effects on the global electronic structure, in particular device efficiency and noise. In this work, we measure single dopant fluctuations which give rise to variations in the surface potential of a mesoscopic metal-insulator-semiconductor (MIS) capacitor device. The MIS device is composed of a metallic frequency-modulated atomic force microscopy (fm-AFM) tip, a vacuum gap, and a multilayer MoSe₂ semiconducting sample.

The energy of a classical capacitor is found by summing the energies of the charge distributions of each capacitor plate:

$$U_{ts} = \frac{1}{2} \left(\int_t \rho_t(z) V_t(z) \partial\tau_t + \int_s \rho_s(z) V_s(z) \partial\tau_s \right) \quad (1)$$

where the first term is the energy of the top electrode (in this case, the fm-AFM tip) and the second term is the energy of the bottom electrode (MoSe₂ sample). For a metal-insulator-metal capacitor, ρ and V are spatially invariant, and the expression simplifies to $U_{ts} = \frac{1}{2} Q_{ts} V_{ts} = \frac{1}{2} C_{ts} V_{ts}^2$. Q_{ts} and V_{ts} are linear with applied bias and C_{ts} is solely geometric. Deviations from a purely metallic system, such as upon introduction of static charges[8], sample or tip polarizability[9, 10], and surface or interface dipoles[11, 12] can cause ρ and V to vary spatially and have a non-linear bias dependence. This is the case for semiconducting samples, where the surface potential V_S that is established by the charge Q_S inside a semiconductor is bias-dependent and spatially non-uniform (thus the potential that arises due to band bending.) In this

work, V_S has been calculated by numerically solving the following equation[13]:

$$V_S = V_{bias} + V_{CPD} - \frac{Q_S}{C_I} \quad (2)$$

where $Q_S = Q_S(V_S)$ and C_I is the (geometric) capacitance per unit area, found by solving the Poisson Equation (see Section I of the Supplemental Material[14] for this derivation). The total charge density is composed of thermal carriers, ionized dopants, and “effective dopants”, which are generically any ionizable states such as surface states, interface traps[15], point vacancies[16], contaminants, adatoms, interstitial atoms[17], etc. This incorporation of ionized “effective dopant” states into the total charge density means that even an undoped sample can behave as though it were doped if other contributing effective dopant densities are appreciable. The occupation of dopant states can vary due to charge transfer from other sample locations, such as the substrate or interstitial contamination layers[18]. The MIS force per unit area a_{tip} (derived in Hudlet *et al* 1995[13]) is:

$$\frac{F_{ts}}{a_{tip}} = \frac{Q_S^2}{2\epsilon} \quad (3)$$

Figures 1a,b show the bias dependence of V_S and F_{ts} , where each data point is a numerical solution to Equations 2 and 3. The non-linear surface potential V_S leads to a nonparabolicity in the force F_{ts} .

In fm-AFM, a tip mounted on a cantilever (spring constant k , Q-factor Q) oscillates sinusoidally above a sample surface ($z = A \sin(\omega t)$). Tip-sample force (F_{ts}) contributions which are in-phase with the cantilever motion lead to shifts in the cantilever resonant frequency ($\Delta\omega$) and out-of-phase force contributions lead to variations in the cantilever drive, or excitation, required to maintain constant oscillation amplitude A :

$$\Delta\omega = \omega - \omega_o = \frac{-\omega_o \omega_o}{2kA} \frac{1}{\pi} \int_0^{2\pi/\omega} F_{ts}(t) \sin(\omega t) \partial t \quad (4a)$$

$$F_d = \frac{kA}{Q} - \frac{\omega_o}{\pi} \int_0^{2\pi/\omega} F_{ts}(t) \cos(\omega t) \partial t \quad (4b)$$

(see Section II of the Supplemental Material[14] for a derivation of Equation 4.) The nonparabolicity in the

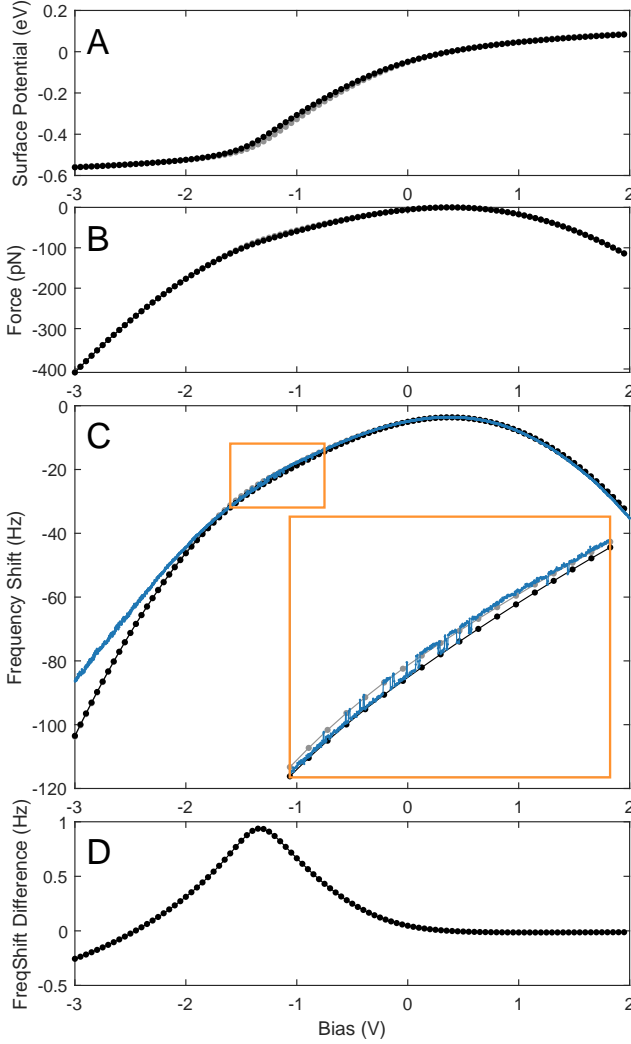


FIG. 1. a) Modelled bias dependence of the MIS surface potential (Equation 2) and b) force (Equation 3) for two ionized acceptor concentrations: $6.3 \times 10^{17}/\text{cm}^3$ (black) and $7.1 \times 10^{17}/\text{cm}^3$ (grey). c) Modelled frequency shift (black and grey, Equation 4a) and fm-AFM frequency shift data (blue) on multilayer MoSe₂. Inset: A zoom-in of the frequency shift (yellow rectangle) for which fluctuations in the data (blue) were observed. d) The difference between the two models (black and grey) shown in a-c, inset as a function of bias. (This is effectively a “noise sensitivity function”.) The experimental and model parameters for (a-d) are given in the main text. The sweep was acquired over approximately 10 seconds, and the bandwidth of the phase-locked-loop was 305 Hz.

force F_{ts} which arises due to the nonlinearity in surface potential V_S leads to a nonparabolic fm-AFM frequency shift above MoSe₂ (Figure 1c). Recently, similar nonparabolicities have been reported in other systems measured with fm-AFM, including dangling bonds on Si(111)[5] and pentacene on KBr[19]. Reference measurements on SiO₂, in contrast, show a parabolic frequency shift as a function of bias. (See Section III of the Supplemental Material[14] for these measurements.)

The inset of Figure 1c shows a zoom-in of the kink in the frequency shift parabola. At these biases, the measured frequency shift (blue) fluctuates between two states. This is due to individual dopant fluctuations which cause variations in Q_S . Notably, what is being measured here is the change in the global electrostatic environment (band bending, V_S) due to this single dopant fluctuation, and not a fluctuating signal arising due to an isolated charge state. This is supported by modelling: The two model fits shown differ only in their acceptor concentration, which are $6.3 \times 10^{17}/\text{cm}^3$ (black) and $7.1 \times 10^{17}/\text{cm}^3$ (grey). This is a dopant concentration difference of $0.8 \times 10^{17}/\text{cm}^3$, which corresponds to approximately one charge within the estimated $2.8 \times 10^{-18} \text{ cm}^3$ tip probing volume, assuming a probe volume equal to the effective tip area ($\pi \times 10^2 \text{ nm}^2$) times the sample thickness (9 nm). This fluctuation effect does not manifest homogeneously over the entire surface; rather, it is only present at certain locations, and vanishes when the tip is moved slightly (50 nm).

The measured frequency shift fluctuation is maximized at biases corresponding to the kink in the surface potential ($\sim -1.4 \text{ V}$). This is demonstrated in Figure 1d, which shows the difference between the two fits in Figure 1c. The model does not include an energy dependence of dopant states. Therefore, Figure 1d signifies that the bias dependence of the fluctuation amplitude is due to an amplification of the measured fluctuating signal at these biases. This occurs because at these biases, the difference between the surface potential in the ionized and un-ionized states is maximized (visualized as the grey and black curves in Figure 1a). See Section IV of the Supplemental Material[14] for a supporting explanation.

Figure 2 shows the excitation signal measured simultaneously with the frequency shift data shown in Figure 1c. The non-constant excitation signifies an out-of-phase tip-sample force F_{ts} , according to Equation 4b. This out-of-phase component arises from charge reorganization inside the sample, or in other words, it is an equilibration timescale for the surface potential. Modeled lag times ranging from 0 to 50 ns are shown in Figure 2a, and the best estimate of this band bending timescale is 30 ns. This timescale is effectively an RC time constant for the tip-vacuum-sample MIS system. An order-of-magnitude estimate of the time constant $\tau = RC$, assuming a simple parallel-plate capacitor $C = \frac{\epsilon\epsilon_0 A}{d}$ and resistivity $\rho = \frac{RA}{d}$, agrees with this model: Using the best-fit relative per-

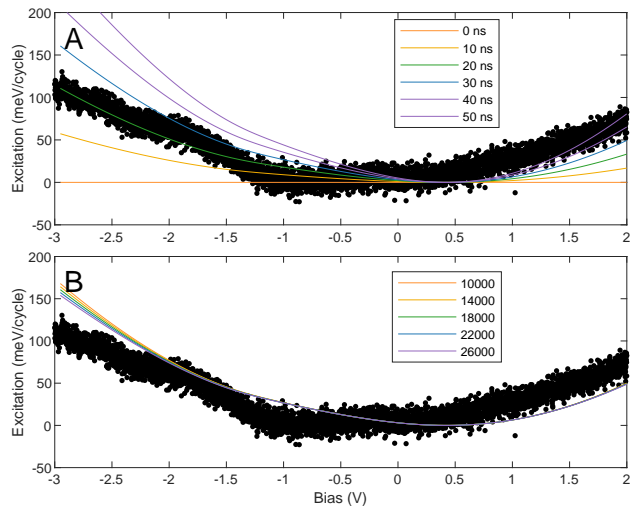


FIG. 2. Modeled excitation signal as a function of bias with a) constant Q -factor (18000); and b) constant lag (30 ns). The other parameters match those defined in the main text. Experimental results taken simultaneously with those shown in Figure 1 are shown in black.

mittivity from this work ($\epsilon = 5.9$) and a resistivity of $500 \Omega m$ (which is within the wide reported resistivity range of $0.1 - 1000 \Omega m$ for MoSe_2 [20]), gives $\tau = 26 \text{ ns}$, which is consistent with the measured 30 ns . The model appears to be simplistic as the fit misses many details of the data. This could be due to a bias-dependent lag time, which has not been accounted for here. Nonetheless this explanation can be useful for an order-of-magnitude estimate of the band-bending timescale. Note that when the lag is zero, the excitation signal is flat, and this is independent of Q . Furthermore, Figure 2b demonstrates that this excitation signal does not arise from variations in Q as a function of bias, since large variations in Q at a constant lag time (30 ns) do not reproduce the measured phenomenon. This confirms that the measured excitation signal is not due to ‘dissipation’ (i.e. a non-conservative force), but rather a time-delayed conservative force. In comparison, reference measurements on SiO_2 , shown in Section III of the Supplemental Material[14] show constant excitation as a function of bias.

The excitation channel can be measured spatially to map variations in band bending timescales over a sample surface. This is demonstrated in Figure 3, which shows frequency shift and excitation bias spectra (a-b) at two locations, as well as frequency shift and excitation images measured at 0 V (c-d) and -1.5 V (e-f). The two positions are separated by approximately 50 nm . The highest layer of the island, susceptible geometrically to the largest surface potential since it is not so spatially limited in the z direction, exhibits the most appreciable bias dependence. Bright spots become visible in the excitation channel, indicating a spatial nonhomogeneity in the charge equilibration time. We note that Figures 3a

and b confirm that this observation of bias-dependent excitation is not a piezoelectric excitation system transfer function artefact such as described in [21], since by changing the position slightly on the sample, the frequency shift and excitation vary independently. This excitation signal is also not due to tunneling charge transfer be-

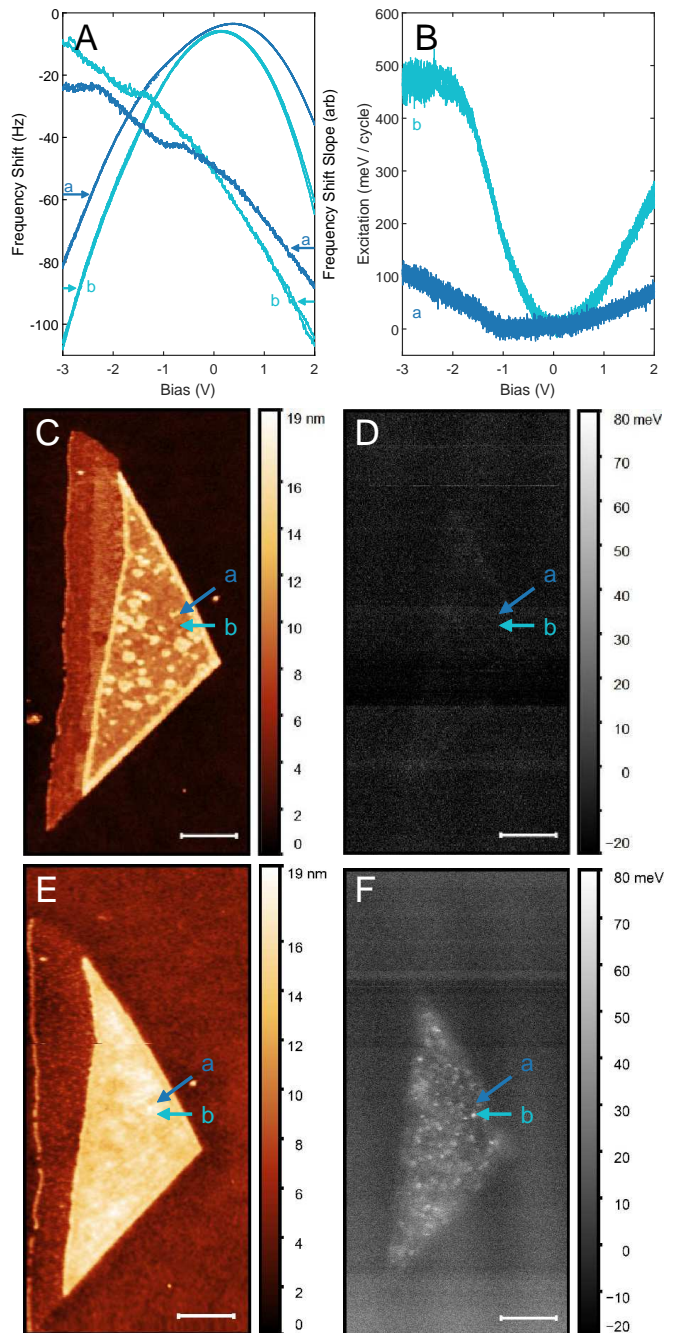


FIG. 3. a,b) Frequency shift and excitation bias spectra acquired at two locations labeled ‘a’ and ‘b’, separated by 50 nm . c,d) Frequency shift and excitation fm-AFM images at 0 V and e,f) -1.5 V . The horizontal scale bar corresponds to 500 nm .

tween the sample and tip, since the effect was observed at tip-sample separations $> 5 \text{ nm}$ larger than that shown in Figure 2.

Model Description – The surface potential, force, frequency shift, and excitation were modelled according to Equations 2, 3, and 4. Over every oscillation cycle, the tip-sample separation changes, the potential drop across the vacuum gap changes, and the potential drop inside the semiconductor changes, resulting in an time-dependent surface potential and force. This time-dependent force is integrated to determine the frequency shift and excitation, where the excitation signal is only non-zero when there is a band-bending timescale, and consequently a phase offset between the closest tip-sample position and the maximum tip-sample force. See Section IV of the Supplemental Material[14] for more detailed explanation of this process, and the Supplemental Material[22] for a video description. Each model point shown in Figures 1a-c and 2 is a numerical solution to Equations 2, 3, and 4 at a different bias.

Model Parameters – Equations 2, 3, and 4 involve 14 experimental parameters. The impact each has on the overall parabola shape is distinct: The band gap, acceptor concentration, permittivity, and temperature introduce nonparabolicity; the tip work function and sample electron affinity introduce lateral shifts and leave the shape unchanged; and the tip-sample separation, tip radius, oscillation amplitude and frequency, spring constant, and Q-factor are all fm-AFM scaling factors that are multiplicative prefactors which do not change the overall shape. See Section V of the Supplemental Material[14] for a further explanation of the sensitivity of each of these parameters and their impact on the shape. Optimal fit values were found by exploring a large parameter space ($> 120,000$ curves) and finding the fit that minimizes residuals. The few-layer MoSe₂ band gap is 1.55 eV [21, 23] (best fit 1.5 eV), electron affinity 3.5 eV [24] (no fit against this parameter), and relative (dielectric) permittivity 5.7 [25] (best fit 5.9). A rigorous interpretation of permittivity is challenging because there is likely water in between the thin flaked MoSe₂ sample and the SiO₂ substrate. However, taking this fitted permittivity as an “effective permittivity” of the net system does not affect the overall interpretation. The effective electron and hole masses were assumed to be 1.0, and the temperature 300 K . The spring constant of 42 N/m estimated by the tip manufacturer agreed with the best fit. The Q-factor 18000 and resonant frequency 330 kHz were measured experimentally by performing a frequency sweep. The oscillation amplitude setpoint, maintained with a phase-locked loop and a feedback circuit, was 6 nm . (The work function of the Si/SiO₂ is 4.4 eV , and given that the substrate parabola peak (i.e. V_{CPD} , see Supplemental Material Section III[14]) is 400 mV , the tip work function ($V_{CPD} = \Phi_{tip} - \Phi_{sample}$) is 4.0 eV (best fit 4.1 eV). The effective tip radius was taken to be 10 nm ,

which is consistent with the tip manufacturer’s estimate of an effective radius “better than 25 nm ”. The optimal closest tip-sample separation z_{ins} was 5.2 nm . The position of the experimental parabola kink at negative biases indicates that the effective dopants are p-type. The dopant concentration, the final fitting parameter, is optimized at $6.3e17/cm^3$ (black) and $7.1e17/cm^3$ (grey). The deviation at large negative biases in Figures 1c-e could be due to the emergence of stray capacitances as the applied electric field increases.

Experimental Parameters – The sample of MoSe₂ on SiO₂ measured in this work was prepared by all-dry viscoelastic stamping[26]. The top layer of the micron-scale multilayer island of MoSe₂ is $9.0 \pm 0.4 \text{ nm}$ above the silicon substrate (see [27] for height measurement methodology.) All fm-AFM measurements were taken using Nanosensors platinum-iridium coated silicon tips (PPP-NCHPt) with 330 kHz resonant frequency, spring constant 42 N/m , and Q factors approximately 18000 in a JEOL JSPM-4500A UHV AFM with a Nanonis control system. All measurements were performed in ultra-high vacuum (base pressure $< 3 \times 10^{-10} \text{ mbar}$) at room temperature. Samples were annealed at 120°C for eight hours after being introduced into vacuum.

In conclusion, we have experimentally demonstrated the direct relationship between a single fluctuating dopant state and its effect on the global band structure (band bending) in a mesoscopic MIS device. The bias dependence of these fluctuations does not depend on the bias dependence of the dopant state occupation, but is rather inherently due to the bias dependence of the surface potential. This has important ramifications for MIS-like device functionality and noise: It indicates that even in the absence of bias dependent dopant or defect states, device noise is bias dependent. The fluctuating two-state effect is demonstrated here for the well-characterized two-dimensional MoSe₂ system, but it has also been observed in pentacene (publication in preparation). This indicates that this is not a sample-specific phenomenon, but rather is relevant for a thorough understanding of noise in any semiconductor device. Additionally, we have demonstrated that band bending equilibration timescales may be measured using the fm-AFM excitation signal. Given that fm-AFM affords high spatial resolution, this approach may be used to directly measure band bending timescales of different types of defects.

We thank NSERC, FRQ-NT and CFI for funding, Alexander Schluger, Kirk Bevan, and Hong Guo for stimulating discussions, and Philipp Nagler for the preparation of the MoSe₂ sample.

[1] L. Gross, F. Mohn, P. Liljeroth, J. Repp, F. Giessibl, and G. Meyer, Measuring the charge state of an

- adatom with noncontact atomic force microscopy, *Science* **324**, 1428 (2009).
- [2] S. Bennett, L. Cockins, Y. Miyahara, P. Grütter, and A. Clerk, Strong electromechanical coupling of an atomic force microscope cantilever to a quantum dot, *Physical Review Letters* **104**, 017203 (2010).
- [3] A. Roy-Gobeil, Y. Miyahara, and P. Grütter, Revealing energy level structure of individual quantum dots by tunneling rate measured by single-electron sensitive electrostatic force spectroscopy, *Nano Letters* **15**, 2324–2328 (2015).
- [4] A. Roy-Gobeil, Y. Miyahara, K. Bevan, and P. Grütter, Fully quantized electron transfer observed in a single redox molecule at a metal surface, *Nano Letters* **19**, 6104–6108 (2019).
- [5] N. Turek, S. Godey, D. Deresmes, and T. Mélin, Ring charging of a single silicon dangling bond imaged by noncontact atomic force microscopy, *Physical Review B* **102**, 235433 (2020).
- [6] K. Teichmann, M. Wenderoth, S. Loth, R. G. Ulbrich, J. K. Garleff, A. P. Wijnheijmer, and P. M. Koenraad, Controlled charge switching on a single donor with a scanning tunneling microscope, *Physical Review Letters* **101**, 076103 (2008).
- [7] R. Plumadore, M. Baskurt, J. Boddison-Chouinard, G. Lopinski, M.n Modarresi, P. Potasz, P. Hawrylak, H. Sahin, F. M. Peeters, and A. Luican-Mayer, Prevalence of oxygen defects in an in-plane anisotropic transition metal dichalcogenide, *Physical Review B* **102**, 205408 (2020).
- [8] L. N. Kantorovich, A. I. Livshits, and M. Stoneham, Electrostatic energy calculation for the interpretation of scanning probe microscopy experiments, *Journal of Physics: Condensed Matter* **12**, 795 (2000).
- [9] S. A. Burke, J. M. LeDue, Y. Miyahara, J. M. Topple, S. Fostner, and P. Grütter, Determination of the local contact potential difference of PTCDA on NaCl: a comparison of techniques, *Nanotechnology* **20**, 264012 (2009).
- [10] J. Zhang, W. Lu, Y. S. Li, J. Cai, and L. Chen, Dielectric force microscopy: Imaging charge carriers in nanomaterials without electrical contacts, *Accounts of Chemical Research* **48**, 1788 (2015).
- [11] M. Schmeits, Electrical conduction in semiconductor junctions with interface dipole layers, *Journal of Applied Physics* **80**, 941 (1996).
- [12] C. León, H. Drees, S. M. Wippermann, M. Marz, and R. Hoffmann-Vogel, Atomic-scale imaging of the surface dipole distribution of stepped surfaces, *Physical Chemistry Letters* **7**, 426–430 (2016).
- [13] S. Hudlet, M. Saint Jean, B. Roulet, J. Berger, and C. Guthmann, Electrostatic forces between metallic tip and semiconductor surfaces, *Journal of Applied Physics* **77**, 3308 (1995).
- [14] See Supplemental Material at <http://link.aps.org/supplemental/placeholder> for relevant derivations of equations in the main text, reference measurements taken on the substrate, an explanation of the sensitivity of the model fit parameters, and an explanation of the fm-AFM signal source, which includes Refs[13, 22–25, 28, 29] (2021).
- [15] M.J. Kirton and M.J. Uren, Noise in solid-state microstructures: A new perspective on individual defects, interface states, and low-frequency (1/f) noise, *Advances in Physics* **38**, 367 (1989).
- [16] H-P. Komsa, J. Kotakoski, S. Kurasch, O. Lehtinen, U. Kaiser, and A. V. Krasheninnikov, Two-dimensional transition metal dichalochenides under electron irradiation: defect production and doping, *Physical Review Letters* **109**, 035503 (2012).
- [17] S-Y. Seo, D-H. Yang, G. Moon, O. F. N. Okello, M. Yeong Park, S-H. Lee, S-Y. Choi, and M-H. Jo, Identification of point defects in atomically thin transition-metal dichalcogenide semiconductors as active dopants, *Nano Letters* **21**, 3341 (2021).
- [18] E. Pollmann, L. Madau, S. Schumacher, U. Kumar, F. Heuvel, C. vom Ende, S. Yilmaz, S. Güngörmüs, and M. Schleberger, Apparent differences between single layer molybdenum disulphide fabricated via chemical vapour deposition and exfoliation, *Nanotechnology* **31**, 505604 (2020).
- [19] Z. Schumacher, R. Rejali, M. Cowie, A. Spielhofer, Y. Miyahara, and P. Grütter, Charge carrier inversion in a doped thin film organic semiconductor island, *ACS Nano* **15**, 10377–10383 (2021).
- [20] X. Zhu, Z. Zhou, Y. Wang, L. Zhang, A. Li, F. Huang, Determining factor of MoSe₂ formation in Cu(In,Ga) Se₂ solar cells, *Solar Energy Materials & Solar Cells* **101**, 57 (2012).
- [21] A. Labuda, Y. Miyahara, L. Cockins, and P. Grütter, Decoupling conservative and dissipative forces in frequency modulation atomic force microscopy, *Physical Review B* **84**, 125433 (2011).
- [22] See Supplemental Material at <http://link.aps.org/supplemental/placeholder> for a video animation of Figure 5 in the main text. (2021).
- [23] Y. Miyahara, J. Topple, Z. Schumacher, and P. Grütter, Kelvin probe force microscopy by dissipative electrostatic force modulation, *Physical Review Applied* **4**, 054011 (2015).
- [24] L.N. Kantorovich and T. Trevelyan, General theory of microscopic dynamical response in surface probe microscopy: From imaging to dissipation, *Physical Review Letters* **93**, 236102 (2004).
- [25] H. Hölscher, B. Gotsmann, W. Allers, U. D. Schwarz, H. Fuchs, and R. Wiesendanger, Measurement of conservative and dissipative tip-sample interaction forces with a dynamic force microscope using the frequency modulation technique, *Physical Review B* **64**, 075402 (2001).
- [26] A. Castellanos-Gomez, M. Buscema, R. Molenaar, V. Singh, L. Janssen, H. S. J. van der Zant, and G. A. Steele, Deterministic transfer of two-dimensional materials by all-dry viscoelastic stamping, *2D Materials* **1**, 01102 (2014).
- [27] R. Plougmann, M. Cowie, Y. Benkirane, L. Schüe, Z. Schumacher, and P. Grütter, How high is a MoSe₂ monolayer?, Manuscript under review <https://arxiv.org/abs/2109.05354> (2021).
- [28] J. E. Sader, T. Uchihashi, M. J. Higgins, A. Farrell, Y. Nakayama, and S. P. Jarvis, Quantitative force measurements using frequency modulation atomic force microscopy—theoretical foundations, *Nanotechnology* **16**, S94–S101 (2005).
- [29] H. J. Hug and A. Baratof, *Noncontact atomic force microscopy* (Springer International Publishing, 2002) Chap. 20, pp. 395–431.
- [30] J. Lindmayer, Field effect studies of the oxidized silicon surface, *Solid-State Electronics* **9**, 225 (1966).
- [31] S. Sadewasser and T. Glatzel, *Kelvin probe force microscopy: From single charge detection to device char-*

- acterization* (Springer International Publishing, 2018).
- [32] S. Tongay, J. Zhou, C. Ataca, K. Lo, T. S. Matthews, J. Li, J. C. Grossman, and J. Wu, Thermally driven crossover from indirect toward direct bandgap in 2D semiconductors: MoSe₂ versus MoS₂, *Nano Letters* **12**, 5576 (2012).
- [33] Choi, B.K. *et al*, Temperature dependence of band gap in MoSe₂ grown by molecular beam epitaxy, *Nanoscale Research Letters* **12**, 492 (2017).
- [34] B. K. Choi, M. Kim, K-H. Jung, J. Kim, K-S. Yu, and Y. J. Chang, Computational search for two-dimensional MX₂ semiconductors with possible high electron mobility at room temperature, *Nanoscale Research Letters* **9**, 716 (2017).
- [35] Q. Zhang, S. Zhang, B. A. Sperling, and N. V. Nguyen, Band offset and electron affinity of monolayer MoSe₂ by internal photoemission, *Journal of Electronic Materials* **48**, 6446–6450 (2019).
- [36] K-K. Kam, *Electrical properties of WSe₂, WS₂, MoSe₂, MoS₂, and their use as photoanodes in a semiconductor liquid junction solar cell*, Ph.D. thesis, Iowa State University (1982).
- [37] M.K. Agarwal, P.D. Patel, and S.K. Gupta, Effect of doping MoSe₂ single crystals with rhenium, *Journal of Crystal Growth* **129**, 559 (1993).

Supplementary Materials

I. SURFACE POTENTIAL AND FORCE

When a bias is applied to a semiconductor, its finite density of states means that there is a spatially-dependent electric field inside the semiconductor. This causes charge within the semiconductor to re-organize, and creates a spatially dependent potential that decays with distance (band bending). The amount of band bending, that is, the difference between the bulk potentials and the potential at the surface, is the surface potential, and is calculated by solving the Poisson equation:

$$\frac{\partial \vec{E}}{\partial z} = -\nabla^2 V = \frac{\rho}{\epsilon} \quad (5)$$

where the total charge density in the semiconductor ρ is generally taken to be due to the thermally excited carriers ($n(z)$, $p(z)$) and ionized dopants (n_D^+ , n_A^-):

$$\rho = e (n(z) - p(z) + n_D^+ - n_A^-) \quad (6)$$

Imperfect (real-world) samples with surface or defect states, such as edge states, dangling bond states, etc, can have additional carriers contributed by either filling (p_s) or depleting (n_s) defect states, just as dopants do. A robust definition of ρ therefore includes these contributions:

$$\begin{aligned} \rho &= e (n(z) - p(z) + n_D^+ - n_A^- + n_d^+ + n_a^-) \\ &= e (n(z) - p(z) + n_{D,d}^+ - n_{A,a}^-) \end{aligned} \quad (7)$$

such that the Poisson equation is:

$$\frac{\partial \vec{E}}{\partial z} = \frac{e}{\epsilon} (n(z) - p(z) + n_{D,d}^+ - n_{A,a}^-) \quad (8)$$

The charge inside the semiconductor is[13]:

$$Q_s = \text{sgn}(u) \frac{\epsilon \epsilon_o k_B T}{e L_D} \left[e^u - u - 1 + \frac{n_i^2}{N_A^2} (e^{-u} + u - 1) \right]^{1/2} \quad (9)$$

where $u = \frac{eV_s}{k_B T}$ and $L_D = \sqrt{\frac{\epsilon \epsilon_o k_B T}{2 N_A e^2}}$. The surface potential is found by solving the following continuity equation numerically[13]:

$$0 = V_{bias} + V_{CPD} - V_S - \frac{Q_S \times z_{ins}}{\epsilon_o} \quad (10)$$

where $V_{CPD} = E_{f,t} - E_{f,s}$ and $E_{f,t}$ and $E_{f,s}$ are the tip and sample Fermi levels, respectively. Finally, the net tip-sample force is found algebraically given the V_S solution:

$$F_{ts} = a_{tip} \times \frac{Q_S^2}{2\epsilon_o} \quad (11)$$

where $a_{tip} = \pi r_{tip}^2$ is the effective tip area. This derivation is shown in greater detail in Hudlet *et al* (1995)[13]. (Note that the expressions have been modified slightly to account for the fact that this system is p-type, and accounting for the fact that the tip and sample have different Fermi levels.)

II. FREQUENCY SHIFT AND EXCITATION

The following section demonstrates that in an fm-AFM experiment, the frequency shift arises from the in-phase component of the tip-sample force, while variations in excitation arises from the out-of-phase component. (This derivation is also presented elsewhere[23–25, 28], but is included here for clarity.) In the small amplitude limit, an fm-AFM cantilever behaves like a damped, driven harmonic oscillator with equation of motion:

$$m\ddot{z} + \xi\dot{z} + kz = F_{drive} + F_{ts}(z, t) \quad (12)$$

where m is the cantilever mass, ξ is the damping coefficient, k is the spring constant, F_{drive} is the driving force, and $F_{ts}(z, t)$ is the tip-sample interaction force. Rewritten in terms friendlier to an experimentalist, given that the cantilever resonance frequency $\omega_o = \sqrt{\frac{k}{m}}$ and quality factor $Q = \frac{m\omega_o}{\xi}$, we have:

$$k\ddot{z} + \frac{k\omega_o}{Q}\dot{z} + k\omega_o^2 z = \omega_o^2(F_{drive} + F_{ts}(z, t)) \quad (13)$$

We can solve the equation of motion using the ansatz $z = A\sin(\omega t)$. The drive, which when optimized is 90 degrees out of phase with the position, is $F_{drive} = F_d \cos(\omega t)$, such that:

$$F_{ts}(t) = \left[\frac{kA}{\omega_o^2}(\omega_o^2 - \omega^2) \right] \sin(\omega t) + \left[\frac{kA\omega\omega_o}{\omega_o^2 Q} - F_d \right] \cos(\omega t) \quad (14)$$

The total force F_{ts} can be generically expressed as a Fourier series with the orthonormal basis of $\sin(t)$ and $\cos(t)$. Taking only the terms at frequency ω , we find that the force can be expressed as:

$$F_{ts}(t) = F_{in} \sin(\omega t) + F_{out} \cos(\omega t) \quad (15)$$

where the amplitudes of the in-phase and out-of-phase force contributions are the Fourier coefficients:

$$F_{in} = \frac{\omega}{\pi} \int_0^{2\pi/\omega} F_{ts}(t) \sin(\omega t) \partial t \quad (16a)$$

$$F_{out} = \frac{\omega}{\pi} \int_0^{2\pi/\omega} F_{ts}(t) \cos(\omega t) \partial t \quad (16b)$$

Therefore we can separate Equation 14 into its orthogonal components and rearrange to find the frequency shift ($\Delta\omega$) and drive amplitude (F_d) given any generic tip-sample interaction F_{ts} in the regime where $\omega \approx \omega_o$:

$$\Delta\omega = \omega - \omega_o = \frac{-\omega_o}{2kA} \frac{\omega_o}{\pi} \int_0^{2\pi/\omega} F_{ts}(t) \sin(\omega t) \partial t \quad (17a)$$

$$F_d = \frac{kA}{Q} - \frac{\omega_o}{\pi} \int_0^{2\pi/\omega} F_{ts}(t) \cos(\omega t) \partial t \quad (17b)$$

Consequently, that component of the tip-sample force that is in phase with the cantilever position shifts the cantilever resonant frequency, and the out-of-phase component of the force contributes to the drive signal. Finally, in the regime where $\omega \approx \omega_o$ the drive signal may be expressed as an energy loss per cycle as[29]:

$$E_{ts} = E_o \left[\frac{F_d - F_{do}}{F_d} \right] \quad (18)$$

where $E_o = \frac{\pi k a^2}{Q}$ is the intrinsic damping loss of a high quality factor oscillator[29] and $F_{do} = \frac{kA}{Q}$ is the offset in Equation 4b. Experimental drive signals are also converted to units of energy loss per cycle given the above expression, where $F_d = A_{exc}$ is the measured drive amplitude Volts and $F_{do} = A_{exco}$ is the drive amplitude in Volts measured in the absence of a tip-sample interaction.

III. SUBSTRATE

Reference bias spectroscopy measurements were taken on the SiO_2 substrate underlying the MoSe_2 sample. The frequency shift, as compared to Figure 1b, is parabolic because Si has a comparatively small band gap of 1.1 eV (see Figure 2a) and a larger total insulator thickness (z_{ins}) due to the SiO_2 overlayer (see Figure 2a). (The larger z_{ins} also explains why the magnitude of the SiO_2 frequency shift is much smaller than on MoSe_2 .) The parabolic frequency shift indicates that there is very little charge reorganization occurring within the material. Therefore, the excitation, as compared to Figure 2 on MoSe_2 , is constant on SiO_2 because there no phase offset between the tip-sample position and the tip-sample force.

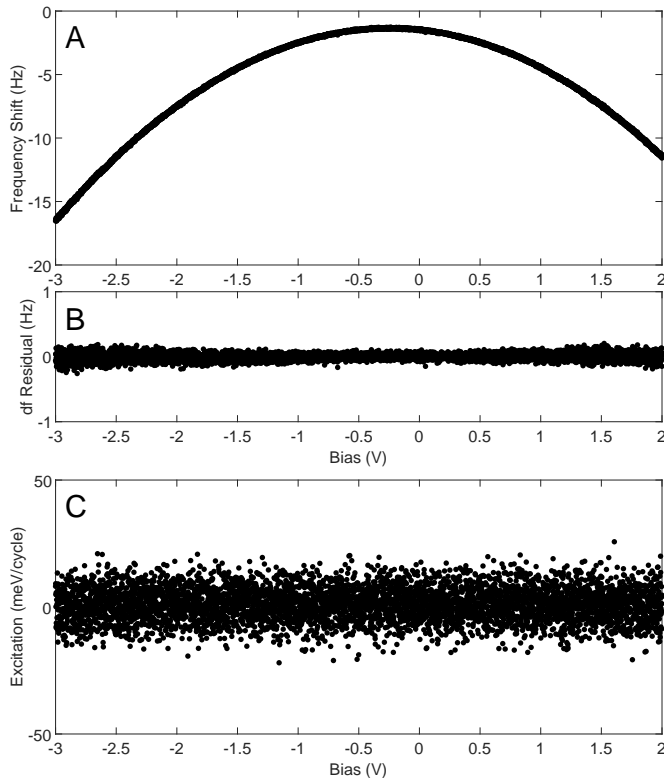


FIG. 4. a) Frequency shift measured on the SiO_2 substrate. b) Residual of the frequency shift and a parabolic fit. c) Excitation measured simultaneously with the frequency shift shown in (a).

IV. FM-AFM SIGNAL SOURCE

To model the frequency shift and excitation channels measured in a fm-AFM experiment, the time-dependent force (which varies over every oscillation cycle, as tip-sample separation z_{ins} varies) must be known. The time-dependent force is calculated by determining the surface potential at varying z_{ins} , according to Equation 2, and then calculating the force according to Equation 3. The z_{ins} and time dependencies of the tip-sample separation, surface potential, and force are shown in Figure 5. An animated version of Figure 5 is provided in the additional Supplemental Material[22]. To calculate the models shown in Figure 1a-b, the $V_S(t)$ and $F(t)$ curves shown in Figure 5 are calculated at varying bias. For each bias, the frequency shift and excitation are calculating by integrating $F(t)$ according to Equation 4.

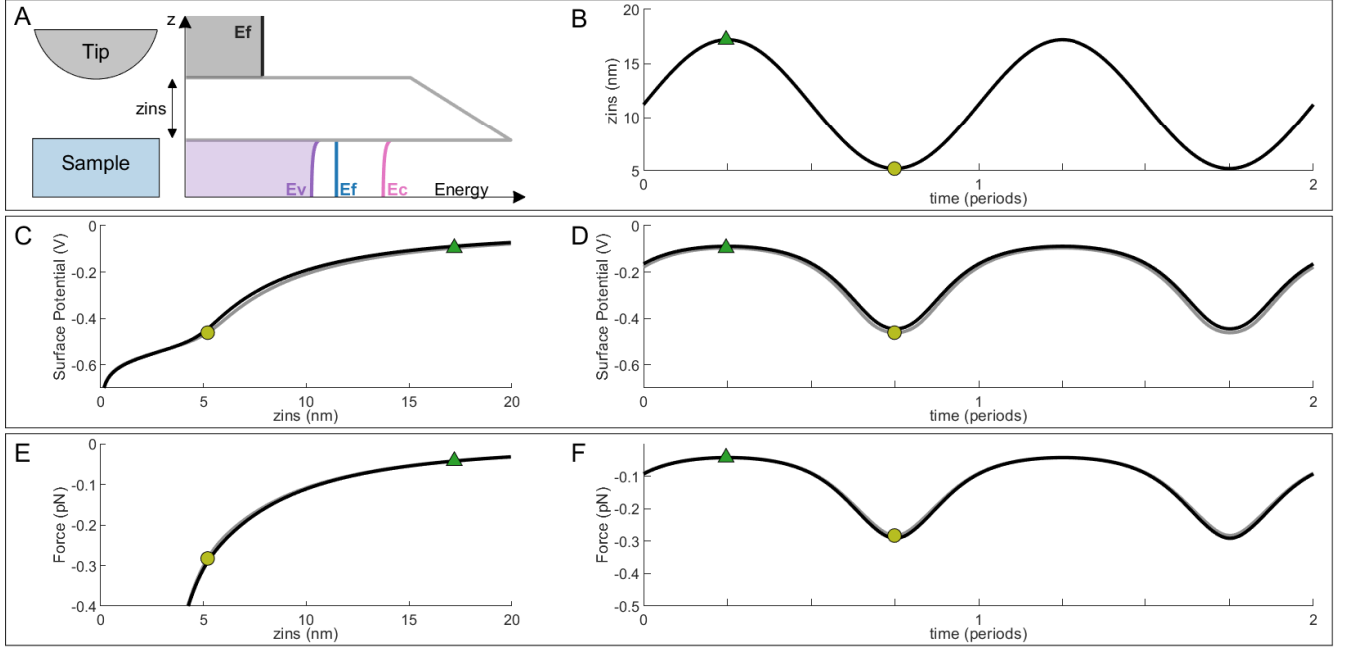


FIG. 5. Simulation of the origin of a fm-AFM force measured over a semiconducting sample at a bias of -1.4 V for two acceptor concentrations: $6.3 \times 10^{17} \text{ cm}^{-3}$ (black) and $7.1 \times 10^{17} \text{ cm}^{-3}$ (grey). (The remaining parameters values are the best fit values defined in the main text.) a) Schematic of the fm-AFM setup corresponding to a band diagram of an MIS capacitor oriented along the z -axis. Pink (E_c) and purple (E_v) are the sample conduction and valence bands, blue (E_f) shows the sample Fermi level, dark grey (E_f) shows metallic tip (gate) Fermi level, and light grey demonstrates the potential drop across the insulator (vacuum). b) Time trace showing that the thickness of the insulator z_{ins} (i.e. tip-sample separation) varies sinusoidally over every oscillation cycle. c,d) The surface potential as a function of z_{ins} and time. e,f) The tip-sample force as a function of z_{ins} and time. Two points, a light green circle and a dark green triangle, are shown for b-f to clarify the relationship between each subfigure. See additional Supplemental Material[22] for an animated version of this figure.

Figure 6 demonstrates how the effects shown in Figure 5 vary with bias. Figures 6a-c show the surface potential as a function of tip-sample separation z_{ins} (dashed) and time (solid) at -2.2 V , -1.4 V , and 1.0 V for two different acceptor concentrations: $6.3 \times 10^{17} \text{ cm}^{-3}$ (black) and $7.1 \times 10^{17} \text{ cm}^{-3}$ (grey). Horizontal lines indicate the surface potential at the closest tip-sample position. Figures 6a-c show that, even though the magnitude of the surface potential swept at -2.2 V exceeds that of -1.4 V , the difference in surface potentials at the closest tip position is larger at -1.4 V . This is significant due to Equation 4a, which shows that the tip-sample force at the closest tip-sample position has the largest contribution to the frequency shift. The integrand from Equation 4a ($F_{ts} \sin(\omega t)$) is found for each acceptor concentration, and their difference is plotted in Figures 6d-f (for -2.2 V , -1.4 V , and 1.0 V , respectively). Figure 6g shows the frequency shift as a function of bias (calculated using Equation 4a), and the biases corresponding to Figures 6a/d, b/e, and c/f (-2.2 V , -1.4 V , and 1.0 V) are highlighted with vertical lines.

This model, therefore, shows that the bias dependence of the frequency shift fluctuation amplitude (Figure 1c) is *not* due to a bias dependence of the dopant state (which has nowhere been incorporated into this model). Rather, it is due to an amplification from the fm-AFM measurement mechanism itself: At biases corresponding to the parabola kink, where the surface potential has the largest nonlinearity, the difference between the ionized state force and the unionized state force is maximized at the closest tip-sample position, leading to the largest difference in frequency

shift.

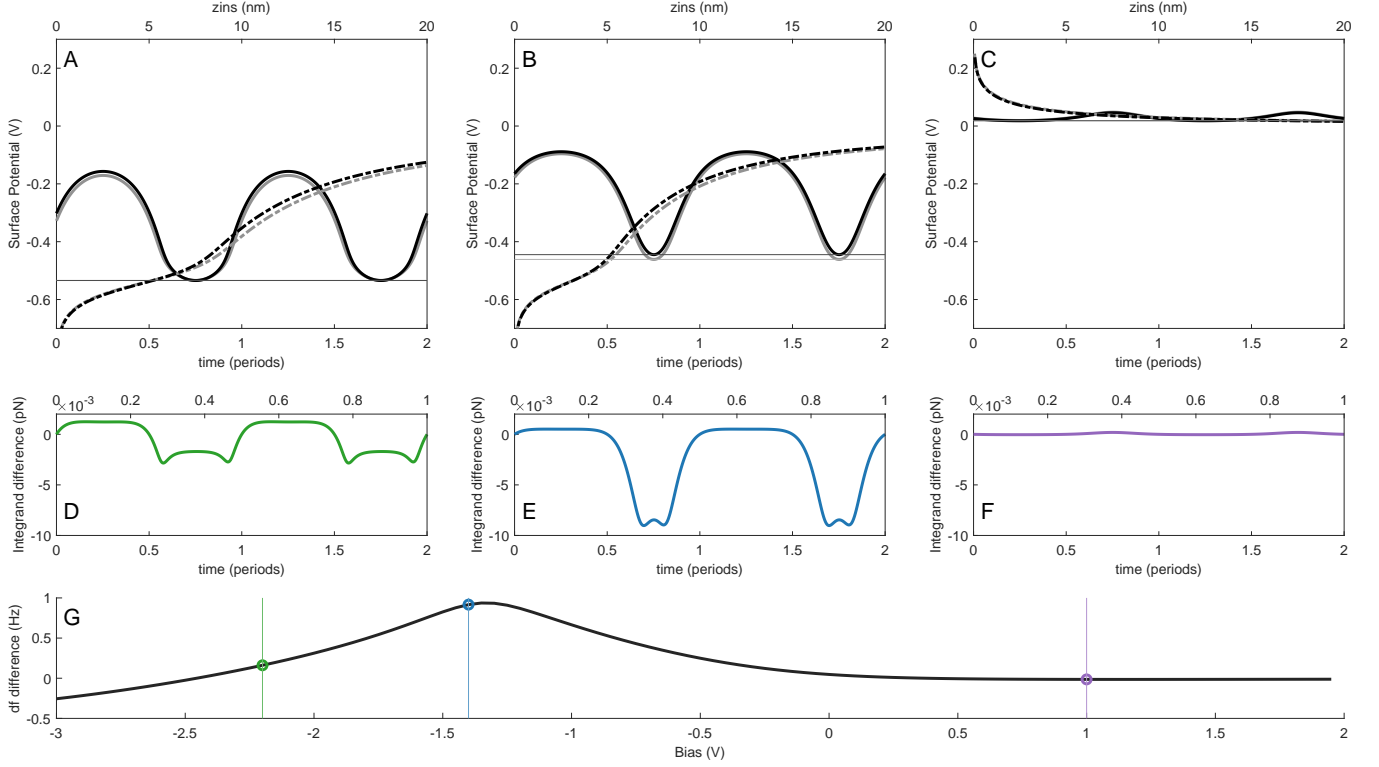


FIG. 6. a,b,c) The surface potential as a function of time (solid) and tip-sample separation z_{ins} (dashed) at $-2.2V$, $-1.4V$, and $1.0V$, respectively. Two different acceptor concentrations are shown: $6.3 \times 10^{17}/\text{cm}^3$ (black) and $7.1 \times 10^{17}/\text{cm}^3$ (grey). Horizontal lines are drawn to indicate the surface potential at the closest tip-sample separation. d,e,f) The force integrand needed to calculate frequency shift ($F_{ts}(t) \sin(\omega t)$, Equation 4a) difference between the two acceptor concentrations as a function of time. for $-2.2V$, $-1.4V$, and $1.0V$, respectively. g) The difference peak (also shown in Figure 1), calculated by integrating $F_{ts}(t) \sin(\omega t)$ as a function of bias. The biases shown in d-f are shown highlighted with vertical lines.

V. FITS

Of the total fourteen experimental parameters in this fit, only three material parameters affect the overall shape of the frequency shift. These are the band gap E_g , acceptor concentration N_A , and permittivity ϵ . The tip work function and sample electron affinity simply provide lateral shifts (Equation 10) in the frequency shift and leave the shape unchanged. There are six fmAFM-specific parameters (tip-sample separation z_{ins} , tip radius r_{tip} , oscillation amplitude A , oscillation frequency ω , spring constant k , and Q-factor Q) which all are simply scaling constants (see Equations 11 and 17a). Slight variations around the best fit values for each of these parameters are shown in Figures 7 and 8, to visually demonstrate the sensitivity of the frequency shift curve to each parameter.

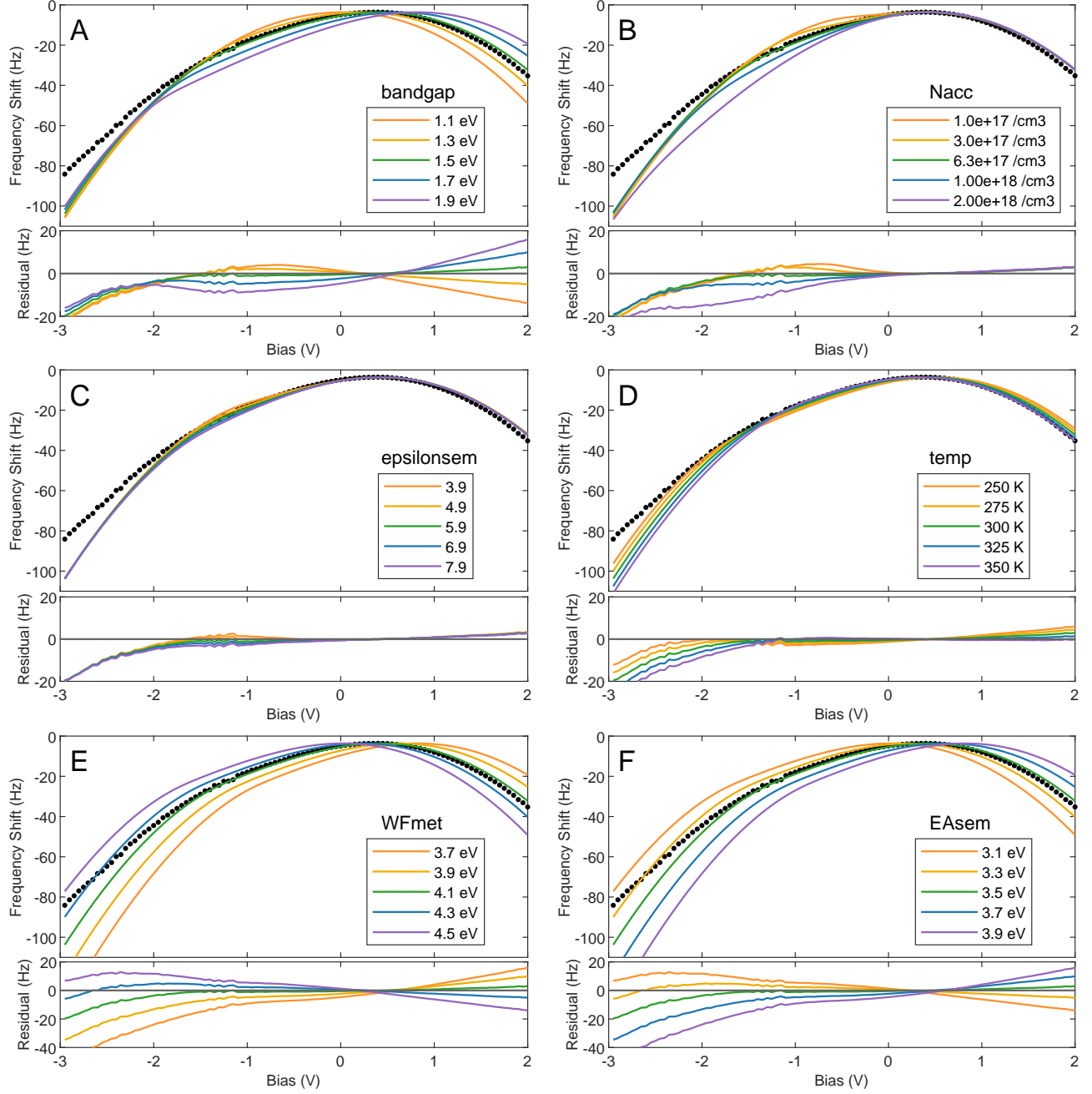


FIG. 7. Visualization of the sensitivity of generic MIS system fit parameters: a) band gap E_g ; b) Acceptor concentration N_A ; c) Permittivity ϵ ; d) Temperature T ; e) Metal work function; f) Semiconductor electron affinity. The data from Figure 1 is shown in black. The best fit values are shown in green.

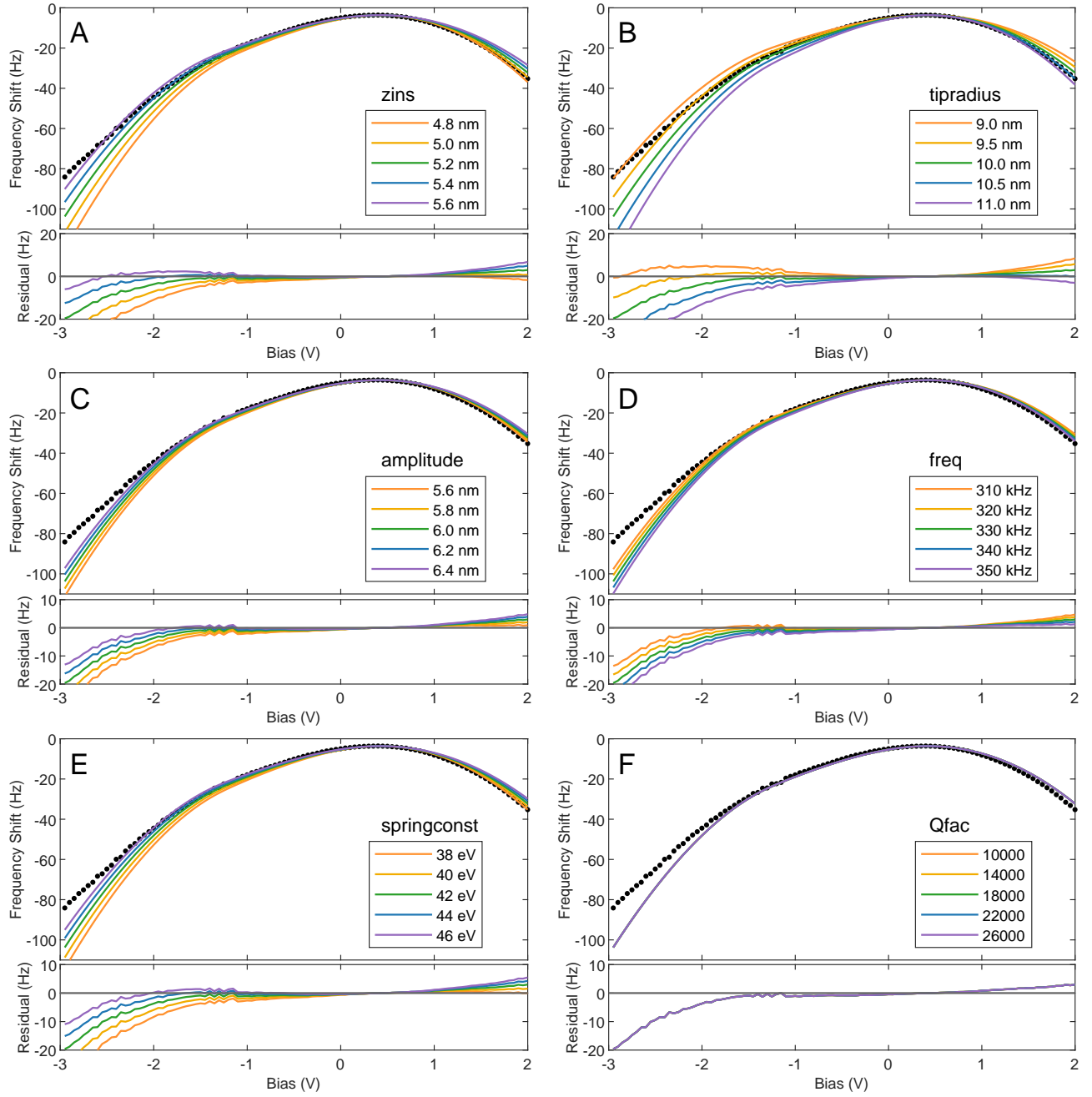


FIG. 8. Visualization of the sensitivity of fm-AFM-specific fit parameters (which are all multiplicative prefactors): a) tip-sample separation z_{ins} ; b) tip radius r_{tip} ; c) oscillation amplitude A ; d) oscillation frequency ω ; e) spring constant k ; f) Q-factor Q (note that Q-factor curves are all perfectly overlapping). The data from Figure 1 is shown in black. The best fit values are shown in green.